Regularized Nonlinear Discriminant Analysis
An Approach to Robust Dimensionality Reduction for Data Visualization

Martin Becker[1,2,3], Jens Lippel[1] and André Stuhlsatz[1]
[1]*Faculty of Mechanical and Process Engineering, University of Applied Sciences Düsseldorf, Münsterstr. 156, 40476, Düsseldorf, Germany*
[2]*Faculty of Electrical Engineering and Information Technology, University of Applied Sciences Düsseldorf, Düsseldorf, Germany*
[3]*Faculty of Media, University of Applied Sciences Düsseldorf, Düsseldorf, Germany*

Keywords: High-dimensional Data, Dimensionality Reduction, Data Visualization, Discriminant Analysis, GerDA, Deep Autoencoder, Deep Neural Networks, Regularization, Machine Learning.

Abstract: We present a novel approach to dimensionality reduction for data visualization that is a combination of two deep neural networks (DNNs) with different objectives. One is a nonlinear generalization of Fisher's linear discriminant analysis (LDA). It seeks to improve the class separability in the desired feature space, which is a natural strategy to obtain well-clustered visualizations. The other DNN is a deep autoencoder. Here, an encoding and a decoding DNN are optimized simultaneously with respect to the decodability of the features obtained by encoding the data. The idea behind the combined DNN is to use the generalized discriminant analysis as an encoding DNN and to equip it with a regularizing decoding DNN. Regarding data visualization, a well-regularized DNN guarantees to learn sufficiently similar data visualizations for different sets of samples that represent the data approximately equally good. Clearly, such a robustness against fluctuations in the data is essential for real-world applications. We therefore designed two extensive experiments that involve simulated fluctuations in the data. Our results show that the combined DNN is considerably more robust than the generalized discriminant analysis alone. Moreover, we present reconstructions that reveal how the visualizable features look like back in the original data space.

1 INTRODUCTION

Mapping high-dimensional data – usually containing many redundant observations – onto 1, 2 or 3 features that are more informative, often is a useful first step in data analysis, as it allows to generate straightforward data visualizations such as histograms or scatter plots. A fundamental problem arising in this context is that there is no general answer to the question of how one is supposed to choose or even design a mapping that yields these informative features. Finding a suitable mapping typically requires prior knowledge about the given data. At the same time, knowledge is what we hope to be able to derive after mapping the data onto informative features. Frequently, one might know nothing or only very little about the given data. In any case, one needs to be very careful not to mistake crude assumptions for knowledge, as this may lead to a rather biased view on the data. So in summary, it appears as a closed loop "knowledge ⇒ mapping ⇒ informative features ⇒ knowledge", where each part ultimately depends on the given data and the only safe entry point is true knowledge.

Deep neural networks (DNNs) have been proven capable of tackling such problems. A DNN is a model that covers an infinite number of mappings, which is realized through millions of adjustable real-valued network parameters. Rather than directly choosing a particular DNN mapping, the network parameters are gradually optimized (DNN *learning*) with respect to a criterion that indicates whether or not a mapping of a given dataset is informative. Two DNNs that have been shown to be able to successfully learn useful data visualizations are the **Ge***ne***r***alized* **D***iscriminant* **A***nalysis* (GerDA) and **D***eep* **A***uto***E***ncoders* (DAEs) as suggested by (Stuhlsatz et al., 2012) and (Hinton and Salakhutdinov, 2006), respectively. A closer look at these two DNNs reveals that the ideas of what the term "informative" means can be very different.

GerDA is a nonlinear generalization of *Fisher's* **L***inear* **D***iscriminant* **A***nalysis* (LDA) (Fisher, 1936)

Becker M., Lippel J. and Stuhlsatz A.
Regularized Nonlinear Discriminant Analysis - An Approach to Robust Dimensionality Reduction for Data Visualization.
DOI: 10.5220/0006167501160127
In *Proceedings of the 12th International Joint Conference on Computer Vision, Imaging and Computer Graphics Theory and Applications (VISIGRAPP 2017)*, pages 116-127
ISBN: 978-989-758-228-8

and thus considers discriminative features to be most informative, which appears as a very natural strategy to generate well-clustered visualizations of labeled data sets. DAEs, on the other hand, seek to improve an encoder/decoder mapping

$$f_{\mathrm{DAE}} := f_{\mathrm{dec}} \circ f_{\mathrm{enc}}, \tag{1}$$

where f_{enc} is a dimensionality reducing encoder (the desired feature mapping) and f_{dec} is the associated decoder. Practically, this is achieved by defining a criterion that measures the dissimilarity between the data and the reconstructions obtained by encoding and subsequent decoding. DAEs can therefore be learned without the use of class labels. Here, reconstructable features are considered to be most informative.

The novel **Re***gularized* **N***onlinear* **D***iscriminant* **A***nalysis* (ReNDA) proposed in this paper uses the combined criterion

$$J_{\mathrm{ReNDA}} := (1-\lambda)J_{\mathrm{GerDA}} + \lambda J_{\mathrm{DAE}} \quad (\lambda \in [0|1]), \tag{2}$$

where the two subcriteria J_{GerDA} and J_{DAE} are based on GerDA and a DAE, respectively. As the name suggests, we expect the associated ReNDA DNN to be better regularized. Regularization is a well-known technique to improve the generalization capability of a DNN. Regarding dimensionality reduction for data visualization, a good generalization performance is indicated by a reliably reproducible 1D, 2D or 3D feature mapping. In other words, a well-regularized DNN guarantees to learn sufficiently similar feature mappings for different sets of samples that represent the data approximately equally good. Clearly, such a robustness against fluctuations in the data is essential for real-world applications.

Indeed, based on the belief that a feature mapping learned by a DNN should be as complex as necessary and as simple as possible, regularization of DNNs is traditionally imposed in the form

$$J_{\mathrm{effective}} := J_{\mathrm{obj}} + \lambda J_{\mathrm{reg}} \quad (\lambda \in [0|\infty)), \tag{3}$$

which looks very similar to the combined criterion (2). Here, λ is a hyperparameter that is adjusted to control the impact of a regularization term J_{reg} on the DNN's true objective J_{obj}. Well-known approaches following (3) are *weight decay* (encouraging feature mappings that are more nearly linear) and *weight pruning* (elimination of network parameters that are least needed) (cf. (Duda et al., 2000)). Both these measures are intended to avoid the learning of overly complex mappings. The advantage of (2) over these two approaches is that both subcriteria are themselves informative as regards the given data, whereas in most cases, weight decay or pruning can only tell us what we already know: The present DNN covers overly complex feature mappings.

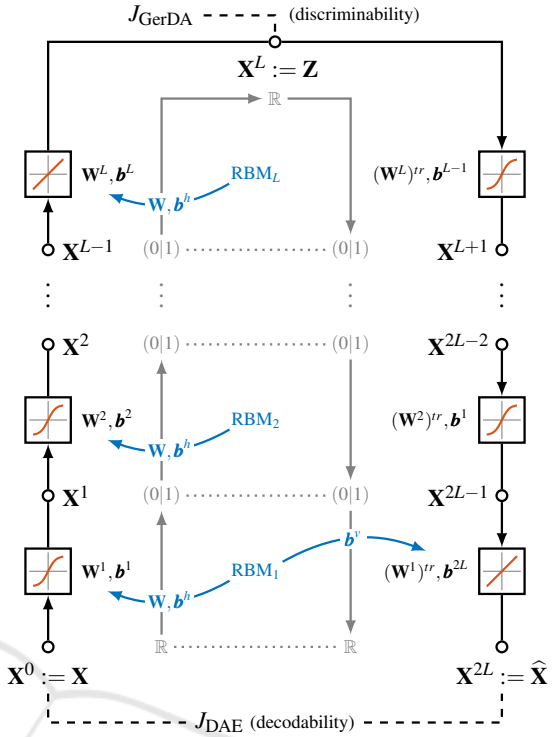

Figure 1: A data flow graph of the overall $2L$-layered ReNDA DNN. Each layer is depicted as a box containing a symbolic plot of its activation function. The L layers on the lefhand side form the encoding and the L layers on the righthand side form the decoding DNN (cf. Sections 2.1 and 2.2). The inner "spaces flow graph" along with the RBMs and the curved arrows concern the RBM-pretraining (cf. Section 2.3). The GerDA criteron J_{GerDA} is connected to feature space node by a dashed line, where it takes direct influence during fine-tuning (cf. Section 2.4). Accordingly, J_{DAE} takes direct influence at original space node and the reconstruction space node.

2 ReNDA

As explained above, ReNDA is a combination of two different DNNs, GerDA and a DAE. As a matter of fact, both these DNNs learn feature mappings in a very similar way, which is another reason why we considered this particular combination: They both use a Restricted Boltzmann Machine (RBM) pretraining to determine good initial network parameters, which are then used for subsequent gradient descent-based fine-tuning. The big difference between them is that a DAE involves an encoding (f_{enc}) and a decoding (f_{dec}) DNN, whereas GerDA involves an encoding DNN only. So contrary to a DAE, GerDA is unable to decode previously learned informative features.

The idea behind ReNDA is to equip GerDA with a suitable decoding DNN and, additionally, introduce it in such a way that it has a regularizing effect on

the encoding GerDA DNN. However, in this paper we focus on presenting the developed ReNDA DNN as a well-regularized and therefore robust approach to data visualization. Figure 1 shows a detailed data flow graph of the overall ReNDA DNN. In the following four subsections we give a detailed explanation of all elements depicted in this figure.

2.1 The Encoding DNN

Suppose that the columns of $\mathbf{X} := (\boldsymbol{x}_1, \ldots, \boldsymbol{x}_N) \in \mathbb{R}^{d_\mathbf{X} \times N}$ are $d_\mathbf{X}$-dimensional samples and that $\boldsymbol{y} := (y_1, \ldots, y_N)^{tr} \in \{1, \ldots, C\}^N$ is a vector of class labels associated with these samples. ReNDA's objective is to find a DNN-based nonlinear encoding

$$\mathbf{X} \mapsto \mathbf{Z} := f_{\text{enc}}(\mathbf{X}) \in \mathbb{R}^{d_\mathbf{Z} \times N} \tag{4}$$

with $d_\mathbf{X} > d_\mathbf{Z} \in \{1,2,3\}$ that is optimal in the sense of an LDA for data visualization, i.e. that the features $\mathbf{Z} = (\boldsymbol{z}_1, \ldots, \boldsymbol{z}_N) \in \mathbb{R}^{d_\mathbf{Z} \times N}$ are both well-clustered with respect to $\boldsymbol{y}$ and visualizable. The layerwise encoding shown on the lefthand side of Figure 1 is obtained by setting $\mathbf{X}^0 := \mathbf{X}$, $d_0 := d_\mathbf{X}$, $\mathbf{X}^L := \mathbf{Z}$, $d_L := d_\mathbf{Z}$ and defining

$$\mathbf{X}^\ell := f_\ell(\underbrace{\mathbf{W}^\ell \mathbf{X}^{\ell-1} + \mathbf{B}^\ell}_{=:\mathbf{A}^\ell(\mathbf{X}^{\ell-1})}) \in \mathbb{R}^{d_\ell \times N} \tag{5}$$

for $\ell \in \{1, \ldots, L\}$ and intermediate dimensions $d_1, \ldots, d_{L-1} \in \mathbb{N}$. We refer to d_0-d_1-d_2-$\cdots$-d_L as the DNN topology. Further, $\mathbf{A}^\ell(\mathbf{X}^{\ell-1}) \in \mathbb{R}^{d_\ell \times N}$ is the ℓth layer's net activation matrix and it depends on the layer's adjustable network parameters: the weight matrix $\mathbf{W}^\ell \in \mathbb{R}^{d_\ell \times d_{\ell-1}}$ and the bias matrix $\mathbf{B}^\ell := (\boldsymbol{b}^\ell, \ldots, \boldsymbol{b}^\ell) \in \mathbb{R}^{d_\ell \times N}$. The function $f_\ell : \mathbb{R} \to \mathbb{R}$ is called the ℓth layer's activation function and it is applied entrywise, i.e.

$$x^\ell_{k,n} = f_\ell(a^\ell_{k,n}(\mathbf{X}^{\ell-1})) \tag{6}$$

for the entries of $\mathbf{X}^\ell$. The encoding DNN's activation functions are set to $f_\ell := \text{sigm}$ with $\text{sigm} : \mathbb{R} \to (0|1)$ given by

$$\text{sigm}(x) := \frac{1}{1+\exp(-x)} \qquad (x \in \mathbb{R}) \tag{7}$$

for $\ell \in \{1, \ldots, L-1\}$ and to $f_L := \text{id}$ with $\text{id} : \mathbb{R} \to \mathbb{R}$ given by

$$\text{id}(x) := x \qquad (x \in \mathbb{R}), \tag{8}$$

respectively. In Figure 1 the activation functions are depicted as symbolic plots.

Altogether

$$f_{\text{enc}} = \underbrace{f_L \circ \mathbf{A}^L \circ \cdots \circ f_2 \circ \mathbf{A}^2 \circ f_1 \circ \mathbf{A}^1}_{\text{layerwise forward propagation}} \tag{9}$$

and optimizing it with respect to J_{GerDA} (cf. Section 2.4.1) corresponds to the originally proposed GerDA fine-tuning (Stuhlsatz et al., 2012). The dashed link between J_{GerDA} and the $\mathbf{Z}$ node of the data flow graph shown in Figure 1 is a reminder that $\mathbf{Z}$ is the GerDA feature space. With the decoding DNN presented in the next section, $\mathbf{Z}$ will become the feature space of the overall ReNDA DNN.

2.2 The Decoding DNN

As can be seen on the righthand side of Figure 1, the adjustable network parameters of ReNDA's encoding DNN are reused for decoding

$$\mathbf{Z} \mapsto \widehat{\mathbf{X}} := f_{\text{dec}}(\mathbf{Z}) \in \mathbb{R}^{d_{\widehat{\mathbf{X}}} \times N} \tag{10}$$

with $d_{\widehat{\mathbf{X}}} := d_\mathbf{X}$. The final biases $\boldsymbol{b}^{2L} \in \mathbb{R}^{d_{2L}}$ represent the only additional network parameters of ReNDA compared to GerDA. We summarize by

$$\boldsymbol{\theta} := (\underbrace{\mathbf{W}^1, \boldsymbol{b}^1, \ldots, \mathbf{W}^L, \boldsymbol{b}^L}_{\substack{\text{network parameters of} \\ \text{the encoding DNN}}}, \boldsymbol{b}^{2L}) \tag{11}$$

the network parameters of the ReNDA DNN. One of the main reasons for this kind of parameter sharing is that it connects f_{enc} and f_{dec} at a much deeper level than (2) alone. Observe that J_{GerDA} and J_{DAE} only take direct influence at three points of the ReNDA DNN. We stated in the introduction that a DNN has typically millions of adjustable real-valued network parameters. So between the two criteria there also lie millions of degrees of freedom. Here, it is very likely that f_{dec} compensates for a rather poor f_{enc} or vice versa. In this case, the two mappings would not be working together. Considering this, we can specify what we mean by a connection of f_{enc} and f_{dec} at a deeper level: The parameter sharing ensures that the two DNNs work on the very same model. It makes the decoding DNN a supportive and complementing coworker that helps to tackle the existing task rather than causing new, independent problems.

We conclude this section with the mathematical formulation of the weight sharing as it is depicted in Figure 1. To provide a better overview, we arranged the layers as horizontally aligned encoder/decoder pairs that share a single weight matrix: Layer $\ell = 2L$ uses the transposed weight matrix $(\mathbf{W}^1)^{tr}$ of the first layer. Layer $\ell = 2L-1$ uses the transposed weight matrix $(\mathbf{W}^2)^{tr}$ of the second layer. So in general,

$$\mathbf{W}^\ell = \left(\mathbf{W}^{2L-\ell+1}\right)^{tr} \tag{12}$$

and $d_\ell = d_{2L-\ell}$ for $\ell \in \{L+1, \ldots, 2L\}$, which implies $d_{2L} = d_0 = d_\mathbf{X} = d_{\widehat{\mathbf{X}}}$. Note that the decoding DNN has the inverse encoding DNN topology d_L-$\ldots$-d_0.

We can therefore still write d_0-$\ldots$-d_L for the DNN topology of the overall ReNDA DNN. In the case of the biases, we see that

$$\boldsymbol{b}^{\ell} = \boldsymbol{b}^{2L-\ell} \tag{13}$$

for $\ell \in \{L+1,\ldots,2L-1\}$. Observe that (13) does not include the additional final decoder bias vector $\boldsymbol{b}^{2L}$ because there is no d_0-dimensional encoder bias vector that can be reused at this point. The symbolic activation function plots indicate that

$$f_{\ell} = \begin{cases} \text{sigm} & L+1 \leq \ell \leq 2L-1 \\ \text{id} & \ell = 2L. \end{cases} \tag{14}$$

Finally, we have that

$$f_{\text{dec}} = f_{2L} \circ \mathbf{A}^{2L} \circ \cdots \circ f_{L+1} \circ \mathbf{A}^{L+1} \tag{15}$$

with $\mathbf{A}^{2L},\ldots,\mathbf{A}^{L+1}$ according to (5). It is

$$\mathbf{X} \mapsto \widehat{\mathbf{X}} = (f_{\text{dec}} \circ f_{\text{enc}})(\mathbf{X}) = f_{\text{DAE}}(\mathbf{X}) \tag{16}$$

and optimizing f_{DAE} with respect to J_{DAE} (cf. Section 2.4.2) corresponds to the originally proposed DAE fine-tuning (Hinton and Salakhutdinov, 2006). Here, J_{DAE} measures the dissimilarity between the samples $\mathbf{X}$ and its reconstructions $\widehat{\mathbf{X}}$. In the data flow graph shown in Figure 1 this is symbolized by a dashed line from the $\mathbf{X}$ node to J_{DAE} to the $\widehat{\mathbf{X}}$ node.

2.3 RBM-Pretraining

As mentioned earlier, both GerDA and DAEs use an RBM-pretraining in order to determine good initial network parameters. In this context, "good" means that a subsequent gradient descent-based fine-tuning has a better chance to approach a globally optimal mapping. Randomly picking a set of initial network parameters, on the other hand, almost certainly leads to mappings that are rather poor and only locally optimal (Erhan et al., 2010). As an in-depth explanation of the RBM-pretraining would go beyond the scope of this paper, we will only give a brief description of the according RBM elements shown in the data flow graph (cf. Figure 1).

Here, we see that there exists an RBM for each horizontally aligned encoder/decoder layer pair. Each RBM_{ℓ} for $\ell \in \{1,\ldots,L\}$ is equipped with a weight matrix $\mathbf{W} \in \mathbb{R}^{d_{\ell-1} \times d_{\ell}}$, a vector $\boldsymbol{b}^{v} \in \mathbb{R}^{d_{\ell-1}}$ of visible biases and a vector $\boldsymbol{b}^{h} \in \mathbb{R}^{d_{\ell}}$ of hidden biases. Once pretrained the weights and biases are passed to the DNN as indicated by the curved arrows. This is the exact same way in which the network parameters of the original GerDA DNN are initialized. Again, the only exception is the final bias vector $\boldsymbol{b}^{2L}$. Here, the bias $\boldsymbol{b}^{v}$ of RBM_1 is used. The initialization of the remaining network parameters of the decoding DNN follows directly from the parameter sharing (12) and (13) introduced in Section 2.2.

2.4 Fine-tuning

Now, for the gradient descent-based fine-tuning we need to specify the two criteria J_{GerDA} and J_{DAE}. It turned out that when combining the two criteria one has to pay attention to their orders of magnitude. We determined the following normalized criteria to be best working.

2.4.1 Normalized GerDA Criterion

Before we present our normalization of the GerDA criterion, we shall review the original criterion

$$Q_z^{\delta} := \text{trace}\big((\mathbf{S}_T^{\delta})^{-1}\mathbf{S}_B^{\delta}\big) \tag{17}$$

as suggested by (Stuhlsatz et al., 2012). Here, it has been shown that maximizing Q_z^{δ} yields well-clustered, visualizable features. The two matrices appearing in (21) are: The weighted total scatter matrix

$$\mathbf{S}_T^{\delta} := \mathbf{S}_W + \mathbf{S}_B^{\delta} \tag{18}$$

with the common (unweighted) within-class scatter matrix $\mathbf{S}_W := (1/N)\sum_{i=1}^{C} N_i \boldsymbol{\Sigma}_i$ of the class covariance matrices $\boldsymbol{\Sigma}_i := (1/N_i)\sum_{n:y_n=i}(\boldsymbol{z}_n - \boldsymbol{m}_i)(\boldsymbol{z}_n - \boldsymbol{m}_i)^{tr}$ with the class sizes $N_i := \sum_{n:y_n=i} 1$ and the class means $\boldsymbol{m}_i := (1/N_i)\sum_{n:y_n=i}\boldsymbol{z}_n$. The weighted between-class scatter matrix

$$\mathbf{S}_B^{\delta} := \sum_{i,j=1}^{C} \frac{N_i N_j}{2N^2} \cdot \delta_{ij} \cdot (\boldsymbol{m}_i - \boldsymbol{m}_j)(\boldsymbol{m}_i - \boldsymbol{m}_j)^{tr} \tag{19}$$

with the global symmetric weighting

$$\delta_{ij} := \begin{cases} 1/\|\boldsymbol{m}_i - \boldsymbol{m}_j\|^2 & i \neq j \\ 0 & i = j. \end{cases} \tag{20}$$

Clearly, δ_{ij} is inversely proportional to the distance between the class means $\boldsymbol{m}_i$ and $\boldsymbol{m}_j$. The idea behind this is to make GerDA focus on classes i and j that are close together or even overlapping, rather than ones that are already far apart from each other.

For ReNDA, we modified Q_z^{δ} as follows:

$$J_{\text{GerDA}} := 1 - \frac{Q_z^{\delta}}{d_{\mathbf{Z}}} \in (0|1) \tag{21}$$

The division through $d_{\mathbf{Z}}$ is the actual normalization (cf. Appendix A). Subtracting this result from one makes J_{GerDA} a criterion that has to be minimized, which is a necessary in order to be able to perform gradient descent for optimization. See Appendix B for the partial derivatives of J_{GerDA}.

2.4.2 Normalized DAE Criterion

During our first experiments, we used the classical mean squared error

$$\mathrm{MSE} := \frac{1}{N} \|\widehat{\mathbf{X}} - \mathbf{X}\|_F^2 \in [0|\infty) \tag{22}$$

with Frobenius norm

$$\|\mathbf{U}\|_F := \sqrt{\sum_{i=1}^{m} \sum_{j=1}^{n} |u_{i,j}|^2} \quad (\mathbf{U} \in \mathbb{R}^{m \times n}) \tag{23}$$

as the DAE criterion. Here, the problem is that the MSE is typically considerably greater than Q_z^δ. Note that (21) implies $Q_z^\delta \in (0|d_\mathbf{Z})$. So in the context of dimensionality reduction for data visualization where $d_\mathbf{Z} \in \{1,2,3\}$ this difference in order of magnitude is especially large. We therefore modified the DAE criterion in the following way:

$$J_{\mathrm{DAE}} := \frac{\mathrm{MSE}/d_\mathbf{X}}{1 + \mathrm{MSE}/d_\mathbf{X}} \in [0|1) \tag{24}$$

The division through $d_\mathbf{X}$ was arbitrarily introduced. Together with N it kind of prenormalizes $\|\cdot\|_F^2$ before the final normalization $(\cdot)/[1+(\cdot)]$. It is part of our future work to find whether or not there exists a better denominator than $d_\mathbf{X}$, or even if there is a better way of defining a normalized DAE criterion.

However, with J_{GerDA} (cf. (21)) and J_{DAE} having the same bounded codomain, their combination is less problematic. The partial derivatives of J_{DAE} can be found in Appendix C.

3 EXPERIMENTS

In the introduction we claimed that DNNs are able to successfully learn dimensionality reducing mappings that yield informative, visualizable features. For both GerDA and DAEs this claim has been experimentally proven: In (Stuhlsatz et al., 2012) and (Hinton and Salakhutdinov, 2006), respectively, the widely used MNIST database of handwritten digits (LeCun et al., 1998) has been mapped into a 2D feature space. In another example, GerDA has been used for an emotion detection task. Here, 6552 acoustic features extracted from speech recordings were reduced to 2D features that allow to detect and visualize levels of valence and arousal (Stuhlsatz et al., 2011).

In the following two sections, we experimentally show that our expectations concerning ReNDA are true, i.e. that ReNDA is also able to successfully learn feature mappings for data visualization and that these mappings are robust against fluctuations in the data, which is due to improved regularization. In order to be able to see this improvement in regularization, we ran all experiments for both ReNDA and GerDA and compared their results.

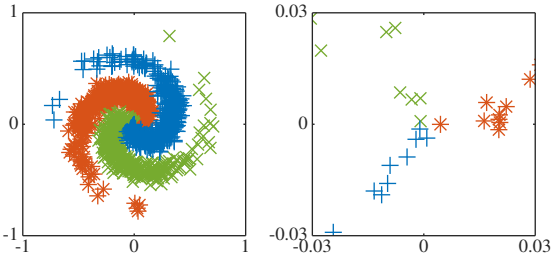

Figure 2: A scatter plot of the artificial galaxy data set. The plot on the righthand side shows a zoom of the center point of the galaxy. Here, we see that the 3 classes are in fact non-overlapping but very difficult to separate.

Throughout all of the ReNDA experiments we set $\lambda = 0.5$, mainly because it avoids prioritization of any of the two criteria J_{GerDA} and J_{DAE} (cf. (2)), i.e. we did not validate λ beforehand. It simply would have been too computationally expensive.

3.1 Artificial Galaxy Data Set

To initially verify the expectations stated above, we used the artificially generated galaxy-shaped data set shown in Figure 2. Although it is already very easy to visualize, DNN learning of optimal 1D features is still challenging. The reason why we chose to use an artificial rather than a real-world data set is that most of the interesting real-world data sets are often far too complex to obtain fast results. In the case of the galaxy data set, the associated DNN parameters are relatively fast to compute, which made it possible to run very extensive experiments but with reasonable computational effort.

3.1.1 Experimental Setup

The main goal of this experiment is to investigate the influence of fluctuations in the data on the learned ReNDA and GerDA visualizations. The results will allow us to compare these two approaches as regards their robustness.

We simulated fluctuations in the data by taking 10 distinct sets of samples from the galaxy data set, which were then used for 10 ReNDA and 10 GerDA runs. In detail, each of the 10 galaxy sets contains 1440 samples (480 per class) that were presented for DNN learning, and additional 5118 samples (1706 per class) that were used for validation. Further details on how the samples are presented for DNN learning can be found in the Appendix D.

For both ReNDA and GerDA we chose the DNN

topology 2-20-10-1. This choice is based on the very similar 3-40-20-10-1 DNN topology that (Stuhlsatz et al., 2012) used to learn informative 1D features from a 3-class artificial Swiss roll data set. Removing the intermediate dimension 40 made DNN learning more challenging while reducing the computational effort. In other words, it yielded a less flexible DNN mapping but with fewer parameters to optimize.

One very important aspect to consider is that the algorithmic implementations of both ReNDA's and GerDA's DNN learning, involve the use of a random number stream. In this experiment we ensured that this stream is the same for all 10 ReNDA and all 10 GerDA runs. The initial network parameters of the RBM-pretraining are also based on this stream, which implies that we do not include any potentially biased parameter initializations. Moreover, any fluctuations in both the ReNDA and the GerDA results are due to the simulated fluctuations in the data only.

3.1.2 1D Visualization

We now compare the 1D mappings obtained from the 10 ReNDA and the 10 GerDA runs. To that end, we use class-conditional histograms as a straightforward method for 1D visualization. This is best explained by directly discussing the results. In order to not get things mixed up, we begin with the ReNDA results shown in Figure 3(a) and discuss the GerDA results (cf. Figure 3(b)) afterwards.

The top row of small plots in Figure 3(a) shows the results of the individual ReNDA runs. Each of these plots includes 3 distinct relative histograms that are based on standardized 1D features associated with the validation samples: One that considers the samples in the red or asterisk ($\ast$) class, a second for the green or cross mark ($\times$) class, and a third for the blue or plus mark ($+$) class. The large plot in Figure 3(a) represents an overlay of all small plots. Note that the axis limits of all 11 plots are identical. Therefore, the overlay plot indicates a high similarity between the learned 1D mappings. Only the order of the 3 classes changes throughout the different ReNDA runs, which is due to the symmetry of the galaxy data set.

The corresponding GerDA histograms shown in Figure 3(b) are organized in the very same way as in Figure 3(a). Especially, two small histograms with the same position in 3(b) and 3(a), respectively, are based on the same 1440 samples for DNN learning and the same 5118 samples for validation. However, here we used differently scaled vertical axes depending on the maximum bar height of each histogram. Observe that only the two bold-framed histograms are similar to the ReNDA histograms. Finally, the GerDA overlay plot shows that the 1D mappings learned by GerDA

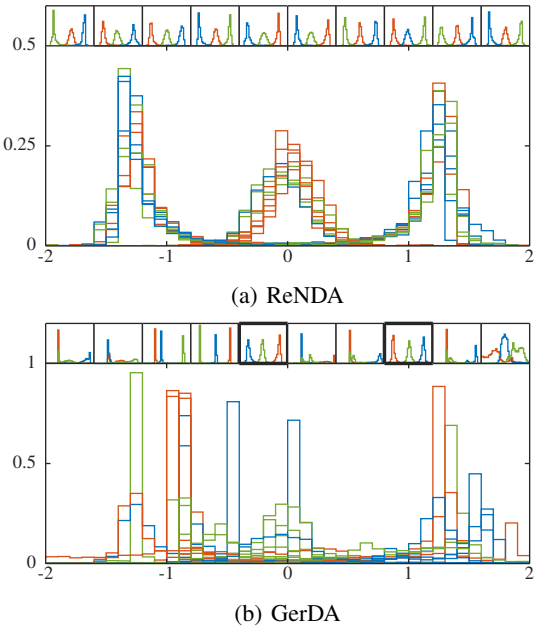

(a) ReNDA

(b) GerDA

Figure 3: A comparison of the 1D mappings learned by ReNDA (a) and GerDA (b). The top row of small subplots in (a) and (b), respectively, shows the histograms of the 1D features associated with the validation samples of each of the 10 galaxy data sets. The large plots represent overlays of these 10 subplots.

are significantly less similar to each other than those learned by ReNDA. In the case of GerDA, the three classes are hardly to detect, whereas for ReNDA we obtained 3 bump-shaped and easy to separate clusters. The latter point, clearly shows that ReNDA is more robust and thus better regularized than GerDA.

3.2 Handwritten Digits

Of course, the artificial galaxy data set used above is neither high-dimensional nor an interesting example from a practical point of view. We therefore decided to run further experiments with the MNIST database of handwritten digits (LeCun et al., 1998), a widely used real-world and benchmark data set for the testing of DNN learning approaches.

MNIST contains a large number of samples of handwritten digits 0 to 9 stored as grayscale images of 28×28 pixels. These samples are organized as two subsets: a *training set* containing 60k samples and a *test set* of 10k samples. Some examples taken from the test set are show in Figure 6(a). With its 28×28 pixel images and variations in the handwriting it falls into the category of big dimensionality data sets as discussed in (Zhai et al., 2014). Nevertheless there are no visible non-understood fluctuations present, which is important for our experimental setup. As before,

we want to simulate the fluctuations in order to see their effect on the feature mappings.

3.2.1 Experimental Setup

The setup of this experiment slightly differs from that of the previous one. We again considered fluctuations in data but also fluctuations in the random number stream that both ReNDA and GerDA depend on (c.f. Section 3.1.1). In practice, the latter fluctuations are especially present when DNN learning is performed on different computer architectures: Here, very much simplified, different rounding procedures may lead to significantly dissimilar mappings even if the same samples are presented for DNN learning.

In this experiment we simulated these fluctuations in the random number stream simply by generating 3 distinct random number streams with a single random number generator. The fluctuations in the data were simulated via 3 distinct random partitions of the 60k training samples into 50k samples presented for DNN learning, and 10k samples for validation. Finally, we combined each of these 3 partitions with each of the 3 random number streams, which then allowed us to realize 9 ReNDA and 9 GerDA runs. Further details on how the samples are presented for DNN learning can be found in Appendix D.

For both ReNDA and GerDA we chose the DNN topology 784-1500-375-750-2 that was also used in (Stuhlsatz et al., 2012) in order to be able to compare our results in a meaningful way.

3.2.2 2D Visualization

In the following we demonstrate ReNDA's improved robustness compared to GerDA by two means: We use 2D scatter plots for data visualization and the class consistency measure DSC suggested by (Sips et al., 2009) to assess the quality and the robustness of the underlying 2D mappings.

The scatter plots in Figure 4(a) show the results of the 9 ReNDA runs. Each column corresponds to 1 of the 3 partitions of the 60k training samples and each row corresponds to 1 of the 3 random number streams as described in the previous section. The 2D features depicted are based on the 10k validation samples of the respective run. Figure 4(b) shows the associated GerDA scatter plots and it is organized in the very same way. This includes that two scatter plots with same position in 4(a) and 4(b) are based on the same combination of a training set partition and a random number stream.

The value given in the bottom left corner of each scatter plot is the associated DSC score. DSC $= 100$ means that all data points have a smaller Euclidean distance their own class centroid than to any other. It is a good measure of visual class separability that can be directly applied to any low-dimensional features even if the underlying original sets of samples are not available. Table 1 presents a comparison of the DSC scores of ReNDA, GerDA and three other approaches to dimensionality reduction for data visualization. Of course, the fact that (Stuhlsatz et al., 2012) achieved a higher DSC score is a less positive result. However, considering the rather high standard deviation within our 9 GerDA runs, this DSC score appears to be a bit misleading, i.e. significantly lower DSC scores are very likely to occur. It is easy to see that ReNDA is much more reliable as regards the DSC score.

Table 1: A comparison of the DSC scores of several DNN approaches to 2D feature extraction from the MNIST data set. The validation results (average $\pm$ standard deviation) for ReNDA and GerDA are based on the 9 DSCs shown in Figure 4(a) and 4(b), respectively. For both ReNDA and GerDA, the test results were obtained by applying the f_{enc} associated with the best validation DSC score on the 10k test samples. In order not only to compare ReNDA and GerDA, we ran all 9 experiments with a *deep belief net* DNN (DBN-DNN) approach suggested by (Tanaka and Okutomi, 2014) (cf. Section 3.2.5). Additionally, the lower table shows the comparison presented by (Stuhlsatz et al., 2012). Here, no validation results were stated.

Our new results		
Learned model	Validation	Test
ReNDA	94.94 ± 0.39	95.03
GerDA	91.47 ± 3.03	93.49
DBN-DNN *	96.62 ± 0.22	96.67
DBN-DNN + LDA *	93.78 ± 4.66	97.00

*) cf. Section 3.2.5

Formerly published results		
Learned model	Validation	Test
t-SNE	n/a	88.99
NNCA	n/a	95.03
GerDA	n/a	96.83

Less evident is the fact that ReNDA again yields reliably reproducible feature mappings. To illustrate that this is nevertheless the case, we suggest a fictive walk through each of ReNDA's scatter plots:

We start at **1** in any scatter plot and walk through the corridor formed by the two clusters **2-3-8-5** and **7-9-4**. Note that [except in the column 2, row 3 plot] both these clusters are arc-shaped or, more precisely, curved towards the path that we are walking on. We stop midway between **4** and **5** and then turn in the direction of the **2-3-8-5** cluster. From here, [except in the column 1, row 2 plot] we first see **6** and then **0**. Here, standing at **0** we would be able to see the other side of the **2-3-8-5** arc.

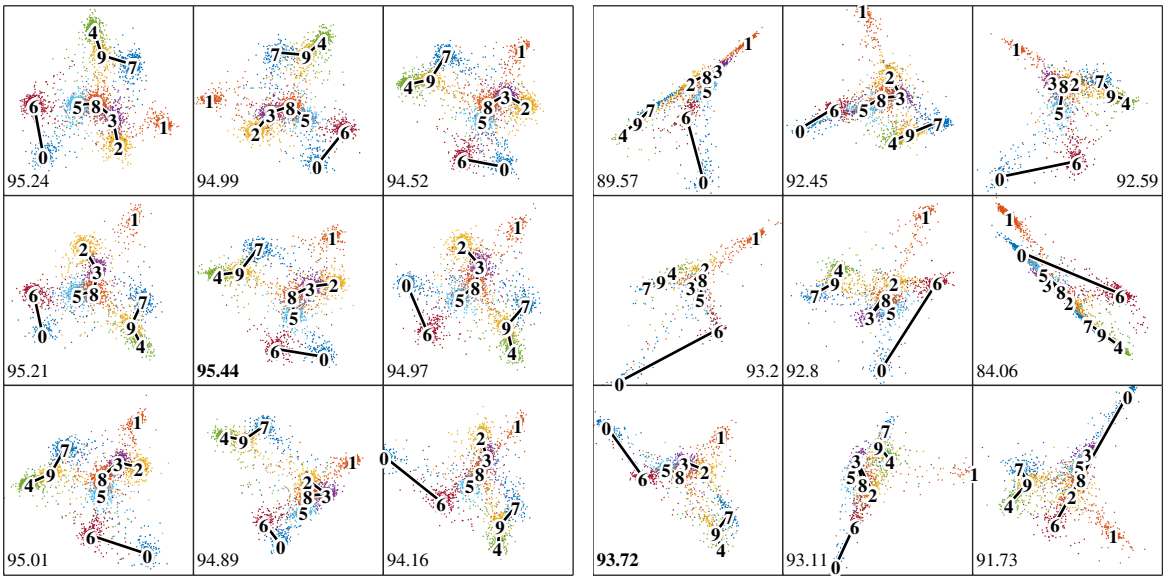

(a) 2D mappings learned by ReNDA (b) 2D mappings learned by GerDA

Figure 4: A comparison of the 2D mappings learned by ReNDA (a) and GerDA (b). In both (a) and (b) the class centroids are marked with the associated digits. Furthermore, clusters of digit classes are indicated by solid black lines. Each column corresponds to 1 of the 3 partitions of the training samples and each row corresponds to 1 of the 3 random number streams. The DSC score of each experiment is placed in the lower left corner.

This walk example shows that relative positions of the classes to each other are very similar from plot to plot. So in conclusion, the simulated fluctuations merely result in rotations and mirrorings of otherwise very similar scatter plots. In the the corresponding GerDA scatter plots (cf. Figure 4(b)), we were unable to visually detect such a high degree of similarity. It again follows that ReNDA is better regularized than GerDA.

3.2.3 Robust Learning Behavior

It is natural to assume that the above final results are due to a more robust, more efficient and more targeted learning behavior. To test this, we compare the two learning curves depicted in Figure 5. The curves show the validation classification error (error for short) as a function of learning epochs, the iterative steps of DNN learning. Clearly, like the DSC score, the error is a measure of class separability. The reason why we use it here is to show ReNDA also performs well on classification tasks.

In detail, we see the average ReNDA error (lower emphasized, **blue** curve) and the average GerDA error (upper emphasized, **red** curve). Both are surrounded by a light gray ribbon indicating the corresponding standard deviation per epoch. The thinner dark gray curves represent the errors of the 9 ReNDA and the 9 GerDA runs, respectively.

Here, the assumed more robust learning behavior of ReNDA is evident because throughout all learning epochs its standard deviation is significantly smaller than that of GerDA. Also its average learning curve is almost constant after epoch 50 whereas GerDA's average learning curve is still falling at epoch 200, which surely can be interpreted as a more efficient and more targeted learning behavior.

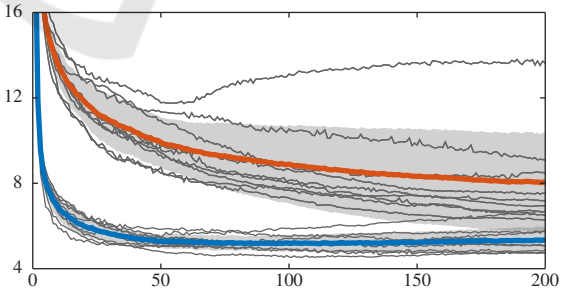

Figure 5: A comparison of the learning curves associated with **ReNDA** and **GerDA**. Each learning curve shows the validation classification error (error for short) as a function of the learning epoch. The lower **blue** and the upper **red** curve represent the average errors. The light gray ribbon surrounding each of the two indicates the corresponding standard deviations per epoch. The thinner dark gray curves show the actual errors per epoch of the 9 ReNDA runs and the 9 GerDA runs.

3.2.4 DAE Reconstruction

In the previous two subsections, we only compared ReNDA and GerDA concerning their robustness. To that end, we looked at 2D scatter plots, DSC scores and learning curves, i.e. views and measures directly associated with the extracted features $\mathbf{Z}$. We will now have a look at the data reconstructions $\widehat{\mathbf{X}}$ that can be obtained from this features.

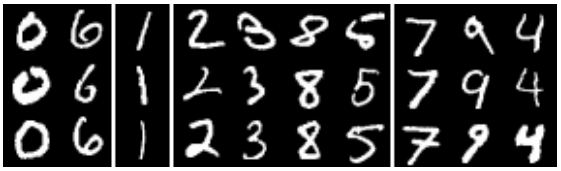

(a) Original MNIST test samples.

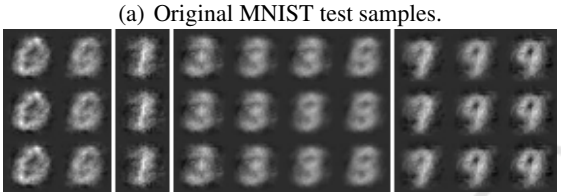

(b) ReNDA, best DSC score

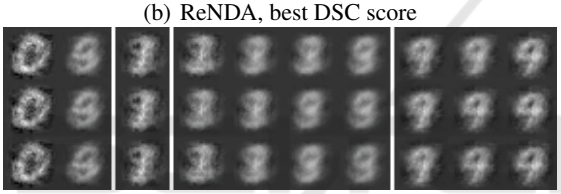

(c) ReNDA, worst DSC score

(d) GerDA, best DSC score

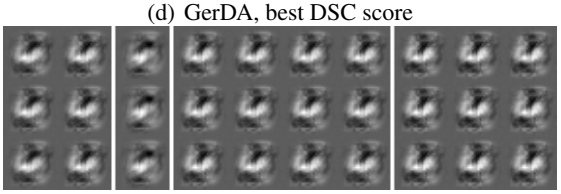

(e) GerDA, worst DSC score

Figure 6: Reconstructions of the MNIST test images, where (a) shows the original samples. The digits are grouped as in Figure 4: **0-6**, **1**, **2-3-8-5** and **7-9-4**. The details on (b) to (e) are given in Section 3.2.4.

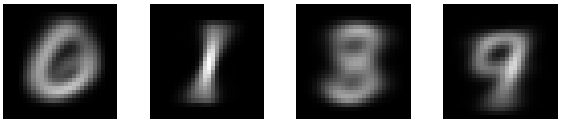

(a) **0-6** (b) **1** (c) **2-3-8-5** (d) **7-9-4**

Figure 7: Average images of all test samples associated with the four clusters **0-6** (a), **1** (b), **2-3-8-5** (c) and **7-9-4** (d) as depicted in Figure 4.

For the reconstructions in Figure 6(b) ReNDA's encoder mapping f_{enc} with the best validation DSC score and its associated decoder mapping f_{dec} were applied on the MNIST test images. For Figure 6(c) we did the same but with ReNDA's worst f_{enc} and its associated f_{dec}. Observe that digits lying in the **7-9-4** cluster have a reconstruction that looks like a blurry 9. In the case of the **2-3-8-5** cluster, it is very similar but with a blurry 3. Clearly, this shows that f_{dec} is able to decode features in a meaningful way, which can be further supported by looking at the means of these clusters (cf. Figure 7). As a matter of fact, the mean images of the **7-9-4** and the **2-3-8-5** cluster are a blurry 9 and a blurry 3, respectively. Another aspect is that these blurry 9s and 3s do not vary much from Figure 6(b) to Figure 6(c). It follows that the decoder mappings are also very robust, which is certainly due to the parameter sharing introduced via (12) and (13) (cf. Section 2.2).

The "reconstructions" shown in Figure 6(d) and Figure 6(e) are based on the GerDA runs with the best and the worst validation DSC score. In order to be able to decode the features, a decoding DNN has been constructed from the learned encoding GerDA DNN via (12) and (13), ReNDA's parameter sharing relations. Further, we have set $\boldsymbol{b}^{2L} = \mathbf{0}$. The result clearly shows that DNN learning of a GerDA DNN generally does not yield suitable network parameters for decoding. At the same time, we have proven that the quality of ReNDA's reconstructions are in fact due to DNN learning of the decoder DNN with respect to the combined criterion J_{ReNDA} (cf. (2)).

A closer investigation reveals that the images in Figure 6(d) are different to those in Figure 6(e) which again indicates that GerDA is not as well-regularized as ReNDA. A very fascinating result is that all digit reconstructions of each of the two GerDA runs appear to be identical, i.e. a learned GerDA DNN assigns the same reconstruction to all digits when constructing a decoder via (12) and (13). The investigation of this phenomenon is a part of our future work.

3.2.5 Comparison with Another DNN

So far, we have only compared ReNDA to its direct predecessor GerDA. In order to be able to provide further comparisons, we ran our 9 experiments with the *deep belief net* DNN (DBN-DNN) approach that has been suggested by (Tanaka and Okutomi, 2014). Though originally designed to infer a binary target vector scheme $y \mapsto \boldsymbol{t} \in \{0,1\}^C$ given by

$$t_i(y) = \begin{cases} 1 & i = y \\ 0 & i \neq y \end{cases} \qquad y \in \{1,\ldots,C\}, \qquad (25)$$

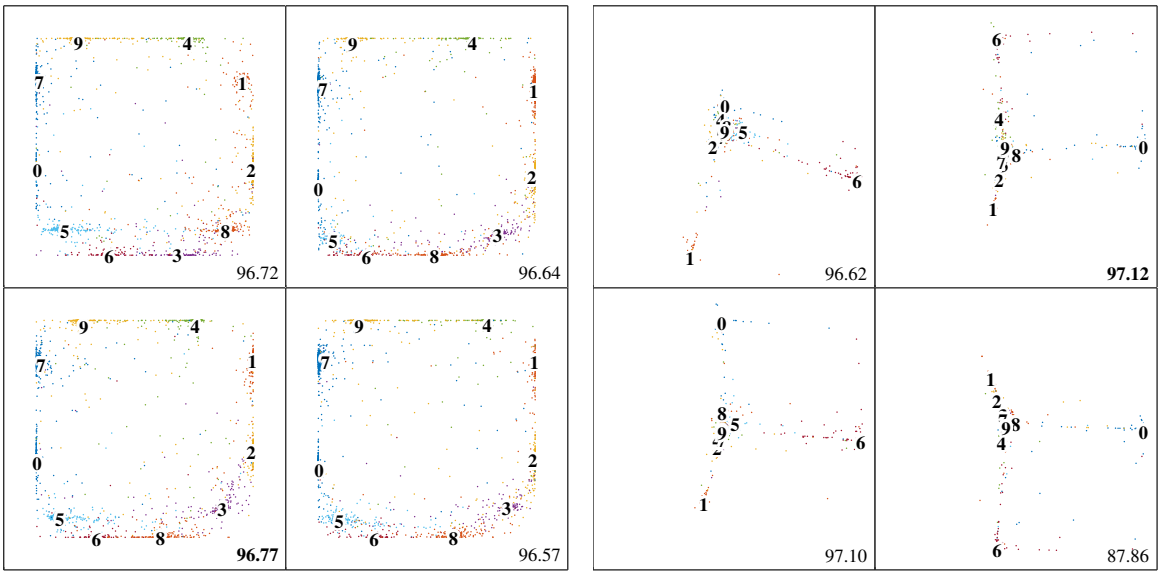

(a) 2D mappings learned by DBN-DNN (b) 2D mappings learned by DBN-DNN + LDA

Figure 8: A comparison of the 2D mappings learned by the DBN-DNN (a) and the DBN-DNN + LDA (b). As in Figure 4 the class centroids are marked with the associated digits. Each column corresponds to first 2 of 3 partitions of the training samples and each row corresponds to first 2 of 3 random number streams. DSC scores are placed in the lower right corner.

we expected it to yield informative, visualizable 2D features. We designed two DBN-DNN experiments, each of which involves the same 9 runs that we used for our ReNDA and GerDA experiments, i.e. we again considered each combination of the 3 partitions of the training samples with the 3 random number streams. Figures 8(a) and 8(b) show the obtained 2D features associated with the 10k validation samples. Because the within class scatter is very small compared to the between class scatter, we decided to show only the four plots corresponding to the first 2 partitions and the first 2 random number streams, respectively. However, the validation results given in Table 1 are based on all 9 runs. The details on the experimental setup can be found in Appendix D.

In our first experiment, we changed the original topology 784-1200-1200-10 (Tanaka and Okutomi, 2014) into 784-1200-1200-2-10, i.e. the intermediate dimension 2 was added in order to obtain visualizable features. As can be seen, the 2D mappings are highly reproducible and the corresponding DSC scores are slightly higher than those of ReNDA. A surprising fact is that the visually separable 2D features tend to lie close to the rim of product set $(0|1) \times (0|1)$. Surely, these particular feature bounds are due to our choice of activation functions: We used $\mathrm{sigm} : \mathbb{R} \to (0|1)$ for all DBN-DNN layers. But the concentration of the features at the rim of the feature space remains an open question.

In our second experiment, we used the original topology 784-1200-1200-10 for DNN learning and applied a classical LDA : $\mathbb{R}^{10} \to \mathbb{R}^2$ dimensionality reduction, afterwards. We refer to this approach as DBN-DNN + LDA (cf. Table 1). Although the DSC scores of the obtained 2D mappings are even higher than those of the above DBN-DNN experiment, the corresponding scatter plots are quiet different to each other. We can therefore conclude that this approach is not as well-regularized as the DBN-DNN and the ReNDA approach. The details on the experimental setup of the DBN-DNN + LDA experiment are given in Appendix D.

4 CONCLUSION

In this paper, we presented and investigated a novel approach to robust dimensionality reduction for data visualization that is a combination of two DNNs: One is a nonlinear generalization of Fisher's LDA called GerDA (Stuhlsatz et al., 2012). The other DNN is a deep autoencoder (DAE) (Hinton and Salakhutdinov, 2006). We refer to the combined DNN as ReNDA (**Re***gularized* **N***onlinear* **D***iscriminant* **A***nalysis*). In the context of data visualization, a well-regularized DNN guarantees to learn a reliably reproducible 1D, 2D or 3D feature representation.

In order to test ReNDAs reliability, we designed extensive experiments with simulated fluctuations in the data. We presented various data visualizations to

show that the learned dimensionality reductions are very useful for information visualization and visual data mining. Here, ReNDA has shown to be more robust against the simulated data fluctuations than GerDA. As far as we know, this paper is the first to present such extensive experiments on the robustness of DNNs. Therefore, we were forced to run all the experiments on our own. Our experiments with the DBN-DNN provide a first glance at the capability of another approach to dimensionality reduction for data visualization (cf. Section 3.2.5). Of course, there are other DNN approaches that are capable of learning informative, visualizable features but here, one must have in mind that extensive experiments are essential to the process of finding suitable DNNs.

In this context, an important task is to figure out what we can learn from other suitable DNNs, e.g. the DBN-DNN (Tanaka and Okutomi, 2014). One of our future task will be to include the recently proposed *drop out regularization* (Srivastava et al., 2014). In addition to the investigation and integration of other promising approaches, there are of course some open questions within the ReNDA approach itself: The most important is if there is a better value for λ than 0.5 and if there is a way to automatically determine an optimal λ-value. The next question points out a chance that comes with ReNDA: Can we exploit the unsupervised learning that the DAE part of ReNDA performs, so that semi-supervised learning tasks can be handled?

In summary, ReNDA has been shown to provide a good way of learning dimensionality reductions for data visualization. Moreover, questions like the two above clearly show that the ReNDA approach can be further advanced and adapted to suit a wide range of real-world applications. Providing the possibility to use ReNDA for semi-supervised learning will be an essential advancement in this context.

ACKNOWLEDGEMENTS

We would like to thank the OVGU Magdeburg, the Faculty of Media (HS Düsseldorf) and the Faculty of Mechanical and Process Engineering (HS Düsseldorf) for providing us with the computational power for our extensive experiments.

REFERENCES

Duda, R. O., Hart, P. E., and Stork, D. G. (2000). *Pattern Classification*. John Wiley & Sons, Inc.

Erhan, D., Bengio, Y., Courville, A., Manzagol, P.-A., and Vincent, P. (2010). Why does unsupervised pre-training help deep learning? *Journal of Machine Learning Research*, 11:625–660.

Fisher, R. A. (1936). The use of multiple measurements in taxonomic problems. *Annals of Eugenics*, 7:179–188.

Hinton, G. E. and Salakhutdinov, R. R. (2006). Reducing the dimensionality of data with neural networks. *SCIENCE*, 313:504–507.

LeCun, Y., Bottou, L., Bengio, Y., and Haffner, P. (1998). Gradient-based learning applied to document recognition. *Proc. of the IEEE*, pages 1–46.

Sips, M., Neubert, B., Lewis, J. P., and Hanrahan, P. (2009). Selecting good views of high-dimensional data using class consistency. *Computer Graphics Forum*, 28(3):831–838.

Srivastava, N., Hinton, G., Krizhevsky, A., Sutskever, I., and Salakhutdinov, R. (2014). Dropout: A simple way to prevent neural networks from overfitting. *Journal of Machine Learning Research*, 15:1929–1958.

Stuhlsatz, A., Lippel, J., and Zielke, T. (2012). Feature extraction with deep neural networks by a generalized discriminant analysis. *IEEE Transactions on Neural Networks*, 666:1–666.

Stuhlsatz, A., Meyer, C., Eyben, F., ZieIke, T., Meier, G., and Schuller, B. (2011). Deep neural networks for acoustic emotion recognition: Raising the benchmarks. In *Proc. IEEE Intern. Conf. on Acoustics, Speech and Signal Processing (ICASSP)*.

Tanaka, M. (2016). Deep neural network. *MATLAB Central File Exchange (# 42853)*. Retrieved Dec 2016.

Tanaka, M. and Okutomi, M. (2014). A novel inference of a restricted boltzmann machine. In *22nd International Conference on Pattern Recognition, ICPR 2014, Stockholm, Sweden, August 24-28, 2014*, pages 1526–1531.

Zhai, Y., Ong, Y. S., and Tsang, I. W. (2014). The emerging "big dimensionality". *IEEE Computational Intelligence Magazine*, 9(3):14–26.

APPENDIX

A. On the Normalized GerDA Criterion

In Section 2.4.1, we stated that the GerDA criterion (21) is normalized, i.e. that $J_{\text{GerDA}} \in (0|1)$. As this is not straightforward to see, we give a proof in this appendix section.

Let λ_k for $k \in \{1,\dots,d_{\mathbf{Z}}\}$ denote the eigenvalues of $(\mathbf{S}_T^{\delta})^{-1}\mathbf{S}_B^{\delta}$. Then $\text{trace}\big((\mathbf{S}_T^{\delta})^{-1}\mathbf{S}_B^{\delta}\big) = \sum_{k=1}^{n}\lambda_k$ and we need to show that $0 < \lambda_k < 1$ for all k.

Therefore, let μ_k for $k \in \{1,\dots,d_{\mathbf{Z}}\}$ denote the eigenvalues of $\mathbf{S}_W^{-1}\mathbf{S}_B^{\delta}$ and let $\boldsymbol{x}_k \in \mathbb{R}^{d_{\mathbf{Z}}}$ denote an eigenvector to the eigenvalue μ_k. Then

$$\begin{aligned} & \mathbf{S}_W^{-1}\mathbf{S}_B^{\delta}\boldsymbol{x}_k = \mu_k \boldsymbol{x}_k \\ \Leftrightarrow \quad & \boldsymbol{x}_k^{tr}\mathbf{S}_B^{\delta}\boldsymbol{x}_k = \mu_k \cdot \boldsymbol{x}_k^{tr}\mathbf{S}_W\boldsymbol{x}_k\,. \end{aligned} \tag{26}$$

Since both $\mathbf{S}_B^\delta$ and $\mathbf{S}_W$ (cf. (19) and (20)) are positive definite, we have that $\mu_k > 0$ for all k. We use (18) to rewrite the characteristic eigenvalue equation associated with (26) as follows:

$$\begin{aligned} & \big(\mathbf{S}_W^{-1}\mathbf{S}_B^\delta - \mu_k \mathbf{I}_{d_\mathbf{Z}}\big)\boldsymbol{x}_k = \mathbf{0} \\ \Leftrightarrow\ & \big(\mathbf{S}_W^{-1}(\mathbf{S}_T^\delta - \mathbf{S}_W) - \mu_k \mathbf{I}_{d_\mathbf{Z}}\big)\boldsymbol{x}_k = \mathbf{0} \\ \Leftrightarrow\ & \big(\mathbf{S}_W^{-1}\mathbf{S}_T^\delta - \underbrace{(\mu_k + 1)}_{=:\kappa_k}\mathbf{I}_{d_\mathbf{Z}}\big)\boldsymbol{x}_k = \mathbf{0} \end{aligned} \tag{27}$$

Clearly, κ_k for $k \in \{1,\ldots,d_\mathbf{Z}\}$ denote the eigenvalues of $\mathbf{S}_W^{-1}\mathbf{S}_T^\delta$ and it is $\kappa_k > 1$ for all k. The eigenvalues of $(\mathbf{S}_W^{-1}\mathbf{S}_T^\delta)^{-1}$ are simply $0 < \kappa_k^{-1} < 1$ for all k. We finally use that $(\mathbf{S}_W^{-1}\mathbf{S}_T^\delta)^{-1} = \mathbf{I}_{d_\mathbf{Z}} - (\mathbf{S}_T^\delta)^{-1}\mathbf{S}_B^\delta$ which is equivalent to (18). With these last two statements we further convert (27) to

$$\begin{aligned} \Leftrightarrow\ & \big((\mathbf{S}_W^{-1}\mathbf{S}_T^\delta)^{-1} - \kappa_k^{-1}\mathbf{I}_{d_\mathbf{Z}}\big)\boldsymbol{x}_k = \mathbf{0} \\ \Leftrightarrow\ & \big((\mathbf{S}_T^\delta)^{-1}\mathbf{S}_B^\delta - \underbrace{\big(1 - \kappa_k^{-1}\big)}_{=\lambda_k}\mathbf{I}_{d_\mathbf{Z}}\big)\boldsymbol{x}_k = \mathbf{0}. \end{aligned} \tag{28}$$

Here, it is easy to see that $0 < \lambda_k < 1$ for all k, which is what we intended to show.

B. Partial Derivatives of $J_{\mathbf{GerDA}}$

Let $\ell \in \{1,\ldots,L\}$. The partial derivatives of J_{GerDA} (cf. (21)) are given by

$$\frac{\partial J_{\text{GerDA}}}{\partial \mathbf{W}^\ell} = \boldsymbol{\Delta}^\ell (\mathbf{X}^{\ell-1})^{tr} \tag{29}$$

$$\frac{\partial J_{\text{GerDA}}}{\partial \boldsymbol{b}^\ell} = \boldsymbol{\Delta}^\ell \cdot \mathbf{1}_N \tag{30}$$

with $\mathbf{1}_N := (1,1,\ldots,1)^{tr} \in \mathbb{R}^N$ and

$$\boldsymbol{\Delta}^\ell := f_\ell'(\mathbf{A}^\ell) \odot \begin{cases} \partial J_{\text{GerDA}}/\partial \mathbf{Z} & \ell = L \\ (\mathbf{W}^{\ell+1})^{tr}\boldsymbol{\Delta}^{\ell+1} & 1 \le \ell < L. \end{cases} \tag{31}$$

It is

$$\frac{\partial J_{\text{GerDA}}}{\partial \mathbf{Z}} = -\frac{1}{d_\mathbf{Z}} \cdot \frac{\partial Q_z^\delta}{\partial \mathbf{Z}}. \tag{32}$$

A computable expression for $\partial Q_z^\delta / \partial \mathbf{Z}$ along with its derivation is given in (Stuhlsatz et al., 2012).

C. Partial Derivatives of $J_{\mathbf{DAE}}$

In the case of J_{DAE} (cf. (24)), the partial derivatives with respect to the weight matrices are given by

$$\frac{\partial J_{\text{DAE}}}{\partial \mathbf{W}^\ell} = \boldsymbol{\Lambda}^\ell (\mathbf{X}^{\ell-1})^{tr} + \big(\boldsymbol{\Lambda}^{2L-\ell+1}(\mathbf{X}^{2L-\ell})^{tr}\big)^{tr} \tag{33}$$

for $\ell \in \{1,\ldots L\}$. The partial derivatives with respect to the bias vectors are given by

$$\frac{\partial J_{\text{DAE}}}{\partial \mathbf{b}^\ell} = \begin{cases} \boldsymbol{\Lambda}^{2L} \cdot \mathbf{1}_N & \ell = 2L \\ (\boldsymbol{\Lambda}^\ell + \boldsymbol{\Lambda}^{2L-\ell}) \cdot \mathbf{1}_N & 1 \le \ell < L. \end{cases} \tag{34}$$

with $\mathbf{1}_N := (1,\ldots,1)^{tr} \in \mathbb{R}^N$. For $\ell \in \{1,\ldots 2L\}$ the matrices $\boldsymbol{\Lambda}^\ell$ are defined by

$$\boldsymbol{\Lambda}^\ell := f_\ell'(\mathbf{A}^\ell) \odot \begin{cases} \partial J_{\text{DAE}}/\partial \widehat{\mathbf{X}} & \ell = 2L \\ (\mathbf{W}^{\ell+1})^{tr}\boldsymbol{\Lambda}^{\ell+1} & 1 \le \ell < 2L. \end{cases} \tag{35}$$

with

$$\frac{\partial J_{\text{DAE}}}{\partial \widehat{\mathbf{X}}} = \frac{2\big(\widehat{\mathbf{X}} - \mathbf{X}\big)}{d_\mathbf{X} \cdot N \cdot (1 + \text{MSE}/d_\mathbf{X})}, \tag{36}$$

which is straightforward to prove.

D. Data Presentation for DNN Learning

The following table contains the details for our experiments with the galaxy data sets and the MNIST data set.

Table 2: Summary of our experiments details: In the case of ReNDA and GerDA, batchsizes and number of epochs were chosen as in (Stuhlsatz et al., 2012). In the case of the DBN-DNN approach, we simply used the default settings from the code provided by (Tanaka, 2016).

ReNDA and GerDA		
Setup / Property	Galaxy	MNIST
Data dimensionality	2	784
Feature dimensionality	1	2
Number of classes	3	10
Number of data samples		
used for DNN learning	1440	50000
used for validation	5118	10000
total, distinct	65580	60000
Pretraining		
Batchsize	144	2000
Number of Epochs	10	50
Fine-tuning		
Batchsize	288	5000
Number of Epochs	1000	200

DBN-DNN and DBN-DNN + LDA *	
Pretraining	
Batchsize	100
Number of Epochs	1000
Fine-tuning	
Batchsize	100
Number of Epochs	1000

(*) only the differences to the ReNDA / GerDA experiments